Linear and nonlinear dynamics of electron fishbones

G. Vlad[1], V. Fusco[1], S. Briguglio[1], C. Di Troia[1], G. Fogaccia[1], F. Zonca[1,2], X. Wang[3]
[1]ENEA, Dipartimento FSN, C. R. Frascati, via E. Fermi 45, 00044 Frascati (Roma), Italy
[2]Institute for Fusion Theory and Simulation and Department of Physics, Zhejiang University, Hangzhou 310027, Peoples Republic of China
[3]Max-Planck-Institut für Plasmaphysik, Boltzmannstrasse 2, D-85748 Garching, Germany
e-mail contact of main author: gregorio.vlad@enea.it

Abstract. Internal kink instabilities exhibiting fishbone like behaviour have been observed in a variety of experiments where a high energy electron population, generated by strong auxiliary heating and/or current drive systems, was present. The results of global, self-consistent, non-linear hybrid MHD-Gyrokinetic simulations will be presented. Linear dynamics analysis will enlighten the effect of considering kinetic thermal ion compressibility and diamagnetic response, and kinetic thermal electrons compressibility, in addition to the energetic electron contribution. Non-linear saturation and energetic electron transport will also be addressed, making extensive use of Hamiltonian mapping techniques, discussing both centrally peaked and off-axis peaked energetic electron profiles. Centrally peaked energetic electron profiles are characterized by resonant excitation and non-linear response of deeply trapped energetic electrons. On the other side, off-axis peaked energetic electron profiles are characterized by resonant excitation and non-linear response of barely circulating energetic electrons which experience toroidal precession reversal of their motion.

1. Introduction

The mutual interaction of particle populations, characterized by very disparate kinetic energies, is of great interest for research on thermonuclear plasmas of fusion relevance, and, in particular, for the so-called "ignited" plasmas, in which the 3.52 MeV α-particles, released in deuterium-tritium (D-T) reactions, have to thermalize by Coulomb collisions with the bulk thermal D-T plasma in order to self sustain its temperature. The interplay of fusion α-particles and magnetohydrodynamics- (MHD), Alfvénic-like modes has been recognized, since long time, as a crucial issue for the success of next generation,"ignited" devices as, e.g., ITER [1]. Indeed, the potential enhancement of the radial transport of energetic particles toward the edge of the plasma device while preventing them to fully thermalize could, in turn, degrade the fusion performance on one side, and damage the plasma facing components on the other. Similar phenomenology could also take place because of energetic particles accelerated by auxiliary heating systems, as, e.g., neutral beam (NB) injection and a variety of radio frequency heating and current drive systems, and, indeed, has been observed in a large selection of present days auxiliary heated toroidal plasma devices (see, e.g., Refs. [2, 3]). One of the "case studies" of energetic particle driven MHD-like modes is the "fishbone" mode, originally observed in the Poloidal Divertor eXperiment (PDX) [4] device, owing its name to the characteristic fishbone-like shape of the perturbed magnetic field signal evolution. The fishbone is an internal kink-like instability driven, in PDX, by energetic ions due to neutral beam injection, which results in anomalous losses of energetic ions themselves. Deeply trapped ions, in presence of a beam deposition profile peaked near the magnetic axis, were recognized to drive the mode [4, 5] because of resonant wave-particle interaction at the energetic particle toroidal precession frequency $\bar{\omega}_{\rm d}$. Fishbone oscillations driven by suprathermal ion population have been observed, since then, on many tokamak devices [2, 3, 6, 7]. Observations indicate that the mode propagates poloidally in the ion diamagnetic drift direction, and toroidally parallel to the energetic particle precession velocity, thus having $\omega \simeq \omega_{\rm res} \simeq \bar{\omega}_{\rm dh}$ and $\omega_{*\rm h}/\omega \simeq \omega_{*\rm h}/\bar{\omega}_{\rm dh} > 0$, consistent with theoretical predictions for unstable modes [5]. Here, $\omega_{\rm res}$ is the resonance frequency, the overbar $\bar{x}$ on the quantity "x" indicates its bounce average, the diamagnetic fre-

quency is $\omega_{*s} = \mathbf{k}\cdot\mathbf{v}_{*s} = \mathbf{k}\cdot\frac{c\mathbf{B}\times\nabla p_s}{n_s e_s B^2} \simeq \frac{nq(r)}{r}\frac{c}{n_s e_s B}\frac{dp_s}{dr}$ and the toroidal drift frequency is $\omega_{\mathrm{d}s} = \mathbf{k}\cdot\mathbf{v}_{\mathrm{d}s} \simeq \frac{nq(r)}{r}\frac{cE_s}{e_s BR}$, with $\mathbf{v}_{*s}$ being the diamagnetic velocity, $\mathbf{v}_{\mathrm{d}s}$ the magnetic drift velocity, "s" indicating the particle species, $\mathbf{k}$ the wave vector, n the toroidal mode number, E_s the energy of the single particle, n_s the density, p_s the pressure, e_s the electric charge, r the minor radius coordinate, B the magnetic field, q the safety factor, and the subscript "h" refers to energetic ("hot") particles. It is worth noting that the ratio $\omega_{*\mathrm{h}}/\bar{\omega}_{\mathrm{dh}}$ does not depend on the sign of the electric charge e_s: thus, deeply trapped energetic electrons with a density profile peaked on-axis and of energy similar to that of energetic ions could be expected to drive a similar fishbone mode, propagating poloidally in the direction of the electron diamagnetic drift, i.e., opposite to the ion fishbone (although with some more unfavorable conditions [8]). The first observation of fishbone oscillations driven by energetic electrons (electron fishbones, or e-fishbones) is reported almost two decades later in DIII-D [9]. In that experiment, strong MHD activity was observed in presence of neutral beam ion heating, in conjunction with off-axis electron cyclotron (EC) current drive and heating on high field side (HFS) and negative central shear equilibria with $q_{\min} \approx 1$. The fishbone oscillations were stronger when EC was applied on the HFS equatorial plane ($\theta_{\mathrm{res}} \approx \pi$, with θ_{res} the resonant poloidal angle of the EC wave absorption location), and decreased while decreasing θ_{res} toward $\theta_{\mathrm{res}} = \pi/2$. From the DIII-D experiment the following conclusions were derived: (1) it was shown that mainly barely trapped energetic electrons with hollow radial density profile were generated slightly internal to the $q_{\min} = 1$ surface; (2) the diamagnetic drift velocity of the energetic electrons (whose sign depends on $\mathrm{sign}(e_s)\nabla p_s$, with $\mathrm{sign}(e_s)$ the sign of the electric charge) is parallel to that of the on-axis peaked energetic ions produced by neutral beams; (3) the orbit averaged toroidal precession velocity (depending on $\mathrm{sign}(e_s)E_s$) of trapped energetic electrons, which is opposite to the one of the energetic ions for deeply trapped particles, reverses its sign when considering barely trapped particles [10, 11], thus becoming parallel to that of deeply trapped energetic ions. As a conclusion, barely trapped energetic electrons with inverted radial density profile could meet the instability condition $\omega_{*\mathrm{Ee}}/\omega \approx \omega_{*\mathrm{Ee}}/\bar{\omega}_{\mathrm{dEe}} > 0$ and drive a fishbone instability, in analogy with deeply trapped energetic ions with on-axis peaked radial density profile (here, the subscript "Ee" stands for "energetic electron"). Later on, other devices observed fishbone oscillations with electron heating only, i.e., electron cyclotron resonant heating (ECRH) and/or lower hybrid heating (LHH) and current drive (LHCD). E-fishbones have linear dispersion relation and excitation mechanisms that are similar to those of energetic ion driven fishbones; moreover, fluctuation induced transport of magnetically trapped resonant particles, due to precession resonance, is expected to depend on energy and not mass of the energetic particles involved, because of the bounce averaged dynamic response [8]. E-fishbones are characterized by a very small ratio between the resonant particle orbit width and the characteristic fishbone length scale ($\sim \delta\boldsymbol{\xi}_r$, the rigid radial kink-type displacement). This is also expected to be the case of ion fishbones in burning plasmas of fusion interest due to the large plasma current in these devices, while this condition is not realized for the energetic ions in present-day experiments. These analogies between e-fishbones in present-day devices and fishbones in burning plasmas provide a practical motivation for investigating these processes, in addition to the general interest of studying e-fishbones "per se".

2. Numerical Simulations

In the following sections we will present the results of numerical simulations performed using the HMGC code [12, 13, 14], which is a hybrid [15] MHD gyrokinetic code originally developed at the ENEA Frascati laboratories. In HMGC, the thermal (bulk) plasma is described

by $O(\epsilon^3)$ non linear reduced MHD equations [16], which describe circular shifted magnetic surface equilibria; moreover, the limit of zero bulk plasma pressure is also assumed; the energetic particles are described by non linear Vlasov equation in the drift-kinetic limit, solved using particle-in-cell technique, the two components (thermal and energetic particles) being coupled [15] via the pressure tensor term of the energetic particle species entering in the extended momentum equation of the bulk plasma. The hybrid scheme allows to consider the effect of the energetic particles on the electromagnetic fields self-consistently, i.e., they are retained non perturbatively. The original version of HMGC has been recently extended to include new physics (XHMGC [17]): diamagnetic effects and thermal ion compressibility are retained in the extended momentum equation of the bulk plasma through the divergence of the thermal ion pressure tensor, obtained by solving the non linear Vlasov equation for that population, in order to account for enhanced inertia response (mostly due to trapped particles) [8, 18, 19] and ion Landau damping [20]. Moreover, XHMGC is able to treat simultaneously, using the kinetic formalism, up to three independent particle populations, assuming different equilibrium distribution functions (as, e.g., bulk ions and electrons, energetic ions and/or electrons accelerated by NB, ICRH, ECRH, fusion alphas, etc.). The XHMGC code has been also used to simulate fishbone modes driven by energetic electrons [21]. As synthetic diagnostic tool, XHMGC allows to follow, in a self-consistent simulation, a set of test particles; the phase-space coordinates of such particles are stored in time, and can be used to compute a variety of single particle physical quantities as , e.g., the single particle frequencies of the supra-thermal electrons, namely, the precession and bounce frequencies. The resonances underlying the linear instability can be clearly identified in this way. Furthermore, the use of energetic particle phase-space diagnostics, based on Hamiltonian mapping techniques [22, 23] generating kinetic Poincaré plots, allow us to isolate the physics processes underlying fishbone mode saturation, frequency chirping and secular (versus diffusive) energetic particle redistribution. The energetic electrons ("Ee") distribution function used in the following simulations is:

$$f_{\mathrm{Ee}} \propto \frac{n_{\mathrm{Ee}}(\psi)}{T_{\mathrm{Ee}}(\psi)^{3/2}} \frac{4}{\Delta\sqrt{\pi}} \frac{\exp\left[-\left(\frac{\cos\alpha-\cos\alpha_0}{\Delta}\right)^2\right]}{\mathrm{erf}\left(\frac{1-\cos\alpha_0}{\Delta}\right)+\mathrm{erf}\left(\frac{1+\cos\alpha_0}{\Delta}\right)} e^{-E/T_{\mathrm{Ee}}(\psi)}\,, \tag{1}$$

where $n_{\mathrm{Ee}}(\psi)$ and $T_{\mathrm{Ee}}(\psi)$ are the radial density and temperature profiles, respectively, E is the single particle energy, α is the pitch angle of the energetic electrons, ψ is the (normalized) poloidal flux, and the parameters α_0 and Δ are used to model the anisotropy in velocity space of the distribution function. In the following simulations performed with XHMGC, the contributions of finite compressibility of thermal ions and thermal electrons will be treated kinetically by considering isotropic Maxwellian distribution functions with $n_{\mathrm{th},j}(\psi)$, $T_{\mathrm{th},j}(\psi)$ being the corresponding density and temperature profiles, with $j = i, e$. We will neglect mode-mode coupling non linearities, thus considering single n toroidal mode number simulations, while particles non linearities will be fully retained.

3. Energetic electrons with density profile peaked on-axis

As a first example of e-fishbone we will consider an energetic electron population with on axis peaked density profile. Similarly to the conventional energetic ion driven fishbones, deeply trapped energetic particles are expected to drive the mode. The same FTU-like equilibrium and scenario of Ref. [21] will be considered in this section (see the above mentioned reference for details). In Ref. [21] it was shown that the e-fishbone mode was destabilized above a certain threshold energetic electron density, propagating poloidally in the direction of the energetic electron diamagnetic velocity (which is, for this equilibrium, also parallel to the bulk

electron diamagnetic velocity), and excited by resonance with deeply trapped energetic electrons ($\omega = \omega_{\rm res} = n\bar{\omega}_{\rm dEe}$). Here, we will reconsider the linear results presented in Ref. [21], where the kinetic contribution of the energetic electrons and bulk ion was considered, by also adding the kinetic contribution of bulk electrons.

Linear dynamics. In this section we will investigate the relative importance of different driving and damping processes accounted for in the model. Following Ref. [17], where the model implemented in XHMGC has been described in detail, let's consider the perpendicular component of the extended MHD momentum equation:

$$\rho_b[\frac{\partial}{\partial t} + (\underbrace{\frac{\mathbf{b}\times\nabla P_{0i\perp}}{\rho_i\omega_{ci}}}_{\text{diamag., bulk ions}} + \delta\mathbf{v}_b)\cdot\nabla]\delta\mathbf{v}_b = -\underbrace{(\nabla\cdot\mathbf{P}_e)_\perp}_{\text{bulk electrons}} - \underbrace{(\nabla\cdot\mathbf{P}_i)_\perp}_{\text{bulk ions}} - \underbrace{(\nabla\cdot\mathbf{P}_{Ee})_\perp}_{\text{en. electrons}} + (\frac{\mathbf{J}\times\mathbf{B}}{c})_\perp\,, \tag{2}$$

where $\delta\mathbf{v}_b$ is the perturbed velocity ($\propto \delta\mathbf{E}\times\mathbf{B}$) of the bulk ions, ρ_i is the bulk ion Larmor radius, ω_{ci} is the ion cyclotron frequency and ρ_b is the mass density $\rho_b = m_i n_i$ of the bulk ions. In Eq. (2) the diamagnetic bulk ion contribution, and the different kinetic contributions coming from the energetic electrons, bulk ions and bulk electrons have been explicitly indicated. In the following simulations the toroidal mode number is $n = 1$, the poloidal Fourier components retained are $m = 1, ..., 6$, normalized resistivity $S^{-1} = 3\times10^5$ and viscosity $\nu\tau_{A0}/a^2 = 3\times10^{-8}$ have been considered to ensure numerical stability (here S is the Lundquist number $S \equiv 4\pi a^2/(\eta c^2\tau_{A0})$, $\tau_{A0} = R_0/v_{A0}$ being the on axis Alfvén time, η the resistivity, $\omega_{A0} \equiv \tau_{A0}^{-1}$ the on axis Alfvén frequency, and a is the minor radius). In figure *1.* the results of a scan in which the strength of the energetic electrons driving term $(\nabla\cdot\mathbf{P}_{Ee})_\perp$ (which is $\propto n_{\rm Ee0}/n_{\rm i0}$) is varied are presented, showing the dependence of the growth rate γ and the frequency ω of the electron fishbone mode on the strength of the drive. Several curves are shown in figure *1.*, corresponding to switching on, one after the other, the contributions highlighted in Eq. (2). First, the divergence of the energetic electron pressure tensor $(\nabla\cdot\mathbf{P}_{Ee})_\perp$, then the diamagnetic bulk ion term $(\mathbf{b}\times\nabla P_{0i\perp})/(\rho_i\omega_{ci})$ and, subsequently, the divergence of the thermal ion pressure tensor $(\nabla\cdot\mathbf{P}_i)_\perp$, which account for the thermal ion Landau damping and generalized inertia, retaining consistently the actual dynamic response of trapped and circulating thermal ions (see also section 2.2 and appendix A of Ref. [8]). Finally, the divergence of the thermal electron pressure tensor $(\nabla\cdot\mathbf{P}_e)_\perp$ is also included (bulk electrons with the same radial density and temperature profiles of thermal ions, with $n_{\rm e0} = n_{\rm i0}$ and $T_{\rm e0} = 7$ keV are considered). The contribution of energetic electrons drives the mode, which has a clear internal kink characteristic with a dominant $m = 1$ component localized, in radius, approximately inside the $q_{\rm min}$ surface $r_{q_{\rm min}}/a \approx 0.35$; the poloidal structure rotates in counter clock wise direction, which corresponds to a mode propagating in the (bulk and energetic) electron diamagnetic velocity direction resulting in a negative real frequency. Referring to the results shown in figure *1.*, we observe that the growth rate increases almost linearly with

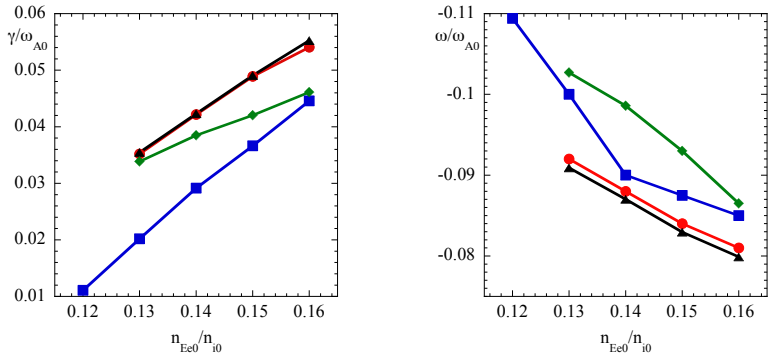

FIG. 1.: Growth rate (left) and frequency (right) of the e-fishbone mode vs. $n_{\rm Ee0}/n_{\rm i0}$. The results are shown of considering only the energetic electron contribution (red circles), and adding, one after the other, the diamagnetic bulk ion contribution (black triangles), the complete bulk ion contribution (blue squares) and the bulk electron one (green diamonds).

the strength of the drive, $\propto n_{\rm Ee0}/n_{\rm i0}$, and the frequency (in absolute value) slightly decreases. When considering also the diamagnetic bulk ion term, very little variation is observed, both in growth rate and frequency: indeed, the absolute value of this term, evaluated at its maximum radial position ($r/a \approx 0.35$) is much less (by a factor ≈ 30) than the absolute value of the frequency of the mode. When adding the term $(\nabla \cdot \mathbf{P}_i)_\perp$, on the contrary, the growth rate of the mode is notably reduced, showing as the effect of considering the thermal ion Landau damping and enhanced inertia increases the threshold in $n_{\rm Ee0}/n_{\rm i0}$ required to destabilize the mode; also the absolute value of the frequency of the mode increases. Finally, when adding the term $(\nabla \cdot \mathbf{P}_e)_\perp$ which accounts for the bulk electrons, an increase of the growth rate is observed, which diminishes its importance as $n_{\rm Ee0}/n_{\rm i0}$ is increased.

Non linear dynamics. The saturation of the e-fishbone driven by energetic electrons with density profile peaked on-axis is characterized by a pronounced downward (in absolute value) frequency chirping, and evident phase locking, as already discussed in Ref. [21]. As a consequence, large radial outward transport of deeply trapped resonant particles is observed, in the region were the linear eigenfunction of the internal kink mode is localized. In figure *2.* the saturation amplitude of the $m, n = 1, 1$ Fourier component of the electrostatic potential $\varphi_{\rm sat\,1,1}$ as the strength of the energetic particle linear drive $\gamma_{\rm L}$ varies, is shown (here ω_0 is the linear frequency). From the simulations we can infer that $|\varphi_{\rm sat\,1,1}| \propto (\gamma_{\rm L}/|\omega_0|)^\lambda$, with $\lambda \approx 2$ for $\gamma_{\rm L}/|\omega_0| \lesssim 0.15$, and $\lambda \lesssim 1$ for $\gamma_{\rm L}/|\omega_0| > 0.15$. These results compare favorably, for weak drive, with the findings of Refs. [24], whereas, for sufficiently strong drive, are in fair agreement with that given in Ref. [25] ($|\delta\boldsymbol{\xi}_r/r_s| \sim |\gamma_{\rm L}/\omega_0|$), noting that $|\delta\boldsymbol{\xi}_r||\omega_0| \sim \mathbf{v}_{\delta\mathbf{E}\times\mathbf{B},r} \sim |\varphi_{1,1}|/r_s$.

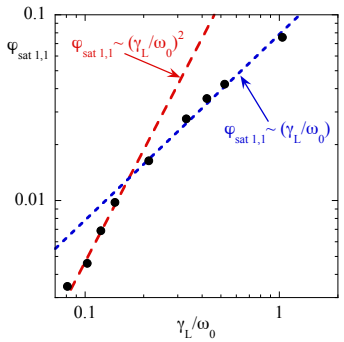

FIG. 2.: Saturation amplitude of $\varphi_{\rm sat\,1,1}$ vs. $\gamma_{\rm L}/\omega_0$ for the peaked on-axis energetic electron density profile.

4. Energetic electrons with density profile peaked off-axis

In this section the first global hybrid MHD-Gyrokinetic simulations of e-fishbones driven by energetic particles with density profile peaked off-axis [26] will be presented. This kind of equilibria is closely related to the experimental configuration in which e-fishbones have been observed in current devices. In these experiments, high field side (HFS) off-axis heating is applied close to the $q_{\rm min}$ flux surface in the equatorial plane, using ECRH; thus, an inverted (positive) gradient of the energetic electron density profile is generated in the radial region of the discharge which is internal to the $q_{\rm min}$ flux surface and in which the internal kink can develop. Moreover, because of the HFS deposition, a selective heating on barely trapped/barely circulating particles will be obtained [9]. Recalling the stability condition, $\omega_{*\rm Ee}/\omega > 0$ [5], and noting that $\omega_{*\rm Ee}$ depends on the sign of the radial gradient of the energetic electron pressure profile, instability can occur only by resonance with energetic electrons characterized by precession reversal; i.e., barely trapped/barely circulating energetic particles [10, 11]. The equilibrium considered here has the same bulk density and temperature profiles and plasma parameters of the peaked on-axis one [21], except for the inverse aspect ratio, $\epsilon = 0.1$, and the safety factor profile q, which also in this case is slightly reversed with $q_0 \approx 1.3$, but with a $q_{\rm min}$ much closer to unity ($\Delta q \equiv 1 - q_{\rm min} = 0.0002$) at the surface $r_{q_{\rm min}}/a \approx 0.33$ and $q_a \approx 5.3$ (see figure *3.* left). Note that $q_{min} \approx 1$ has been used in order to minimize the continuum damping and facilitate the occurrence of the energetic electron driven fishbone [8, 27]. Moreover, safety factor profiles with a reversed shear is known to enhance the

reversal of precessional drift [10, 11, 28]. The profiles of temperatures and densities are shown in figure *3.* right, the on-axis energetic electron temperature being $T_{Ee0} = 50$ keV. The width Δ of the energetic electrons distribution function in the velocity space is $\Delta = 0.5$, whereas $\cos\alpha_0 = 0$ as for the energetic electron density profile peaked on-axis, see Eq. (1). The choice of $\Delta = 0.5$ is such to ensure the presence in the energetic electrons distribution function of a sufficient fraction of barely trapped/circulating particles. Moreover, the choice of a shaped energetic electron temperature profile, which strongly decreases outside the $q \approx 1$ surface, has the beneficial effect of inhibiting the growth of modes with dominant poloidal mode numbers higher than unity, which can be driven unstable by deeply trapped energetic electrons outside the $q = 1$ surface, where the energetic electron density gradient becomes negative.

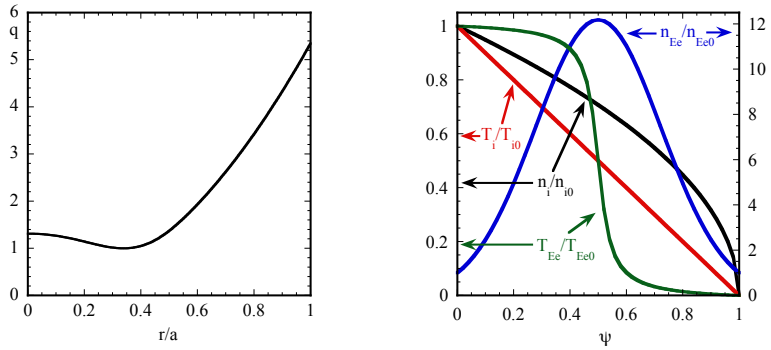

FIG. 3.: Radial profile of the safety factor q vs. r (left) and normalized profiles of $n_{\rm i}(\psi)$, $T_{\rm i}(\psi)$, $n_{\rm Ee}(\psi)$, $T_{\rm Ee}(\psi)$ vs. the flux function ψ (right).

Linear dynamics. The equilibrium described above is unstable above the threshold $n_{\rm Ee0}/n_{\rm i0} \approx 0.007$, showing an almost linear dependence on $n_{\rm Ee0}$ and with a real frequency $\omega_0/\omega_{\rm A0} \approx 0.04$ and very weakly dependent on $n_{\rm Ee0}$. The radial structure of the poloidal Fourier components is dominated by the $m, n = 1, 1$ component, which is localized in the region $q \lesssim q_{\rm min}$, showing the characteristic shape of the internal kink radial displacement. The structure of the mode in the poloidal plane rotates in time in the clock wise direction, i.e., opposite to the direction observed in the peaked on-axis energetic particle radial profile (see the previous section), which corresponds to a mode propagating in the direction of the diamagnetic velocity of the energetic electrons (which is parallel, for a peaked off-axis energetic electrons density profile, to the direction of the bulk ion diamagnetic velocity). Moreover, the frequency of the mode is quite low, as expected for equilibria with low values of Δq (see, e.g., Ref. [27]). From the power exchange between the energetic electrons and wave, as shown in figure *4.*, it is possible to infer which fraction of energetic particles is driving the mode. In figure *4.* (left) the power exchange in the radial shell $0.33 \lesssim r/a \lesssim 0.41$ is shown, with the curves approximating the trapped/untrapped boundary (solid black) and the barely/well circulating boundary (solid red) superimposed. Here, we follow the definition given in Ref. [8] for the barely circulating particles. Indeed, the maximum power exchange occurs for particles in the region of velocity space belonging to that of barely circulating ones (in particular the counter-circulating ones, red pattern), with some minor con-

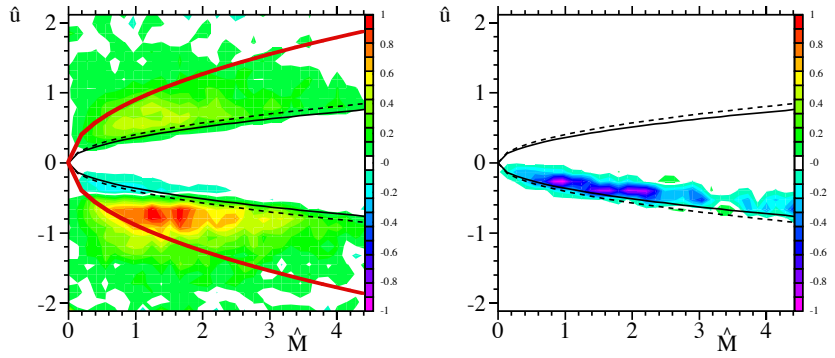

FIG. 4.: Power exchange between energetic electrons and wave, for $n_{\rm Ee0}/n_{\rm i0} = 0.0095$. Contribution from the full population in the radial shell $0.33 \lesssim r/a \lesssim 0.41$ (left), and only trapped particles (right), same radial shell; black lines refer to the boundary between trapped/untrapped particles, whereas solid red curve refers to the boundary between barely circulating and well circulating ones (for $r/a \lesssim 0.41$). Here $\hat{u}$ is the is the parallel velocity normalized to the on-axis Ee thermal velocity and $\hat{M}$ is the magnetic moment M normalized to $T_{\rm Ee0}/\omega_{\rm ce0}$.

tributions coming from the well circulating particles, both co- and counter-circulating (outside the solid red curve, green pattern); trapped particles, on the contrary, give a damping contribution (light blue to dark blue patterns) to the mode, as expected (see figure *4.*, (right) where only the power exchange due to trapped particles is shown in order to enhance the relative size of their contribution). The Hamiltonian mapping technique [22, 23] has been applied to a set of test particles defined by the $C = C_0, M = M_0$ values corresponding to the region where the power exchange between energetic electrons and the wave is maximum in linear phase, i. e., for counter-passing barely circulating energetic particles at $r/a \approx 0.36$, $\hat{u} \approx -0.73$, $\hat{M} \approx 1.55$ (see figure *4.* left), with a frequency of the mode $\omega/\omega_{A0} \approx 0.04$ (here, the quantity $C \equiv \omega_0 P_\phi - nE$, with P_ϕ being the canonical toroidal angular momentum, is a constant of the (perturbed) motion, provided that the perturbed field is characterized by a single toroidal mode number n and a constant frequency). In figure *5.* the radial dependence of the resonant frequency of the circulating test particles $\omega_{\rm res} = n\bar{\omega}_{\rm d} + [\ell + (n\bar{q} - m)\,\sigma]\omega_{\rm b}$, (here, ω_b is the transit frequency) with $l = 0$, $m, n = 1, 1$ and $\sigma = -1$ (counter-passing particles) is compared with the observed frequency of the mode ω_0; also the radial profile of the power exchange between the test particles and the wave is presented, showing how the maximum power exchange corresponds closely to the radii where the test particles are in resonance with the wave. In this case, the resonant condition is satisfied at two radial locations ("double resonance"), as a consequence of the $(q-1)$ term in the resonant condition for circulating particles.

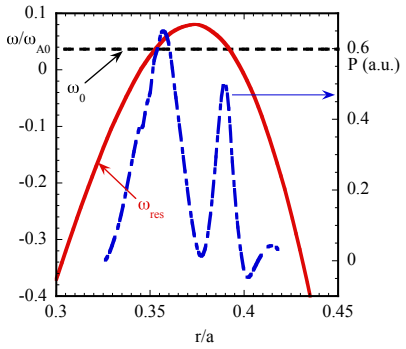

FIG. 5.: Radial dependence of the resonant frequency of the counter-passing barely circulating test particles (solid red curve) compared with the mode frequency ω_0 (dashed black line), for $n_{\rm Ee0}/n_{\rm i0} = 0.0095$, and the test particle power exchange, (blue dot-dashed curve).

Non linear dynamics. In figure *6.* kinetic Poincaré plots are shown, for the test particles belonging to the subset (C_0, M_0) as described in the previous section, with the test particles colored according to their initial P_ϕ value: red color for the particles with $\hat{P}_\phi < \hat{P}_{\phi,\,\rm res1} \approx 125$ (corresponding to $r/a \lesssim r_{\rm res1}/a \approx 0.35$, see figure *5.*), blue color for particles with $\hat{P}_{\phi,\,\rm res1} \lesssim \hat{P}_\phi \lesssim \hat{P}_{\phi,\,\rm res2} \approx 162$ (i.e., $r_{\rm res1}/a \lesssim r/a \lesssim r_{\rm res2}/a \approx 0.39$), and yellow color for particles with $\hat{P}_\phi > \hat{P}_{\phi,\,\rm res2}$ (i.e., $r/a \gtrsim r_{\rm res2}/a$). While entering the fully non linear phase ($t\omega_{A0} \gtrsim 670$, see figure *6.*, third frame from left), we note that the two island structures tend to insinuate oneself into the other, having a P_ϕ extension (or, equivalently, a radial extension) of the order of the distance between the two resonance layers $|P_{\phi,\,\rm res2} - P_{\phi,\,\rm res1}|$. As the test particles are displaced outside the resonant layer (toward $r < r_{\rm res1}$, or $r > r_{\rm res2}$), where the characteristic resonant frequency changes rapidly with radius (see figure *5.*), even changing its sign and, thus, not

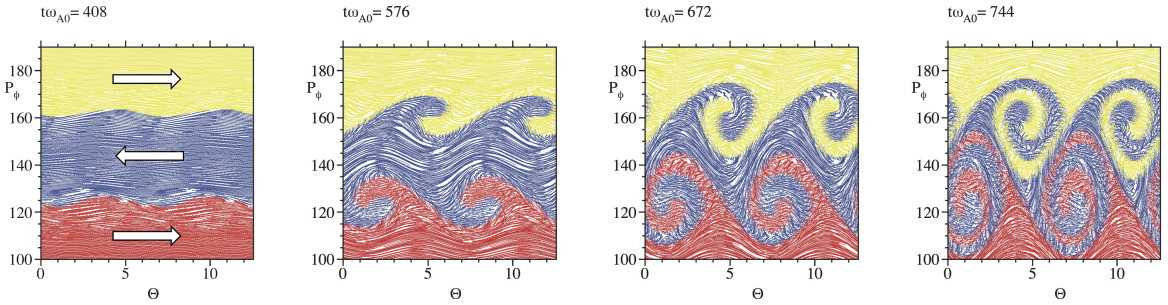

FIG. 6.: Kinetic Poincaré plots for the case of $n_{\rm Ee0}/n_{\rm i0} = 0.0095$, in the plane (P_ϕ, Θ), with Θ the wave-particle phase. Test particles are colored according to their initial P_ϕ values. The arrows in the first plot indicate the direction of the particle drift along Θ above, in between, and below the resonant layers $P_{\phi,\,\rm res} \approx 7$.

satisfying any more the instability condition $\omega_{*\mathrm{Ee}}/\omega > 0$, the mode has no "convenience" in adjusting its frequency to that of the linearly resonant particles. Indeed, little variation of the frequency during the saturation phase is observed, and the saturation of this simulation can be ascribed to "resonance detuning" (see, e.g., Refs. [23, 25, 29, 30]). In figure *7.* the scaling of the saturation amplitude of the electrostatic potential vs. the ratio of the linear growth rate to the frequency of the mode $\gamma_\mathrm{L}/\omega_0$ is shown, in a scan in which the energetic particle density is varied: a stronger scaling, $\varphi_{\mathrm{sat}\,1,1} \approx (\gamma_\mathrm{L}/\omega_0)^3$ is observed for values of $\gamma_\mathrm{L}/\omega_0 \lesssim 0.3$, whereas for larger $\gamma_\mathrm{L}/\omega_0$ the scaling approaches $\varphi_{\mathrm{sat}\,1,1} \approx (\gamma_\mathrm{L}/\omega_0)^{3/2}$. It can be shown that these simulation results compare favorably with the analytic findings obtained in the case of weak energetic particle drive, when the ω_res radial profile has a local maximum at $r = r_s$, $\omega_\mathrm{res}(r_s) \equiv \omega_{\mathrm{res}0}$: in this case, the scaling for the saturated displacement $|\delta\boldsymbol{\xi}_{r0}| \sim \gamma_\mathrm{L}^3 |\omega_0|^{-3/2} |\Delta\omega|^{-3/2} |2\omega_0/\omega''_{\mathrm{res}0}|^{1/2}$ is obtained, when noting that, in the case of $|\Delta\omega| \equiv |\omega_{\mathrm{res}0} - \omega_0| > \gamma_\mathrm{L}$ (corresponding to the low γ/ω values in figure *7.*) that scaling gives $|\varphi_{1,1\,\mathrm{sat}}| \propto |\delta\boldsymbol{\xi}_{r0}||\omega_0| r_s \sim \gamma_\mathrm{L}^3$, whereas for $|\Delta\omega| \sim \gamma_\mathrm{L}$ one gets $|\varphi_{1,1\,\mathrm{sat}}| \propto |\delta\boldsymbol{\xi}_{r0}||\omega_0| r_s \sim \gamma_\mathrm{L}^{3/2}$.

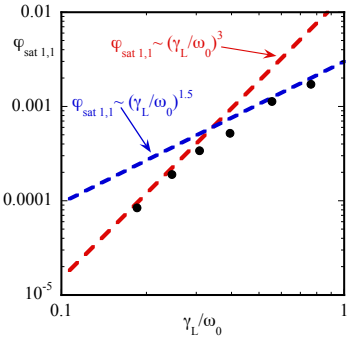

FIG. 7.: Saturation amplitude of $\varphi_{\mathrm{sat}\,1,1}$ vs. $\gamma_\mathrm{L}/\omega_0$ for the peaked off-axis Ee density profile.

Acknowledgements. Useful and stimulating discussions with Liu Chen are gratefully acknowledged. The computing resources and the related technical support used for this work have been provided by CRESCO/ENEAGRID High Performance Computing infrastructure and its staff [31]. This work has been carried out within the framework of the EUROfusion Consortium and has received funding from the Euratom research and training programme 2014-2018 under grant agreement No 633053. The views and opinions expressed herein do not necessarily reflect those of the European Commission.

References

[1] Aymar R, et al. 1997, in *Proceedings of the 16th International Conference on Fusion Energy* 1996, Vol. 1 (International Atomic Energy Agency, Vienna) p. 3.
[2] ITER Physics Basis Editors, et al. 1999 *Nucl. Fusion*, 39 2137.
[3] Fasoli A, et al. Progress in the ITER Physics Basis Chapter 5: Physics of energetic ions 2007 *Nucl. Fusion*, 47 S264.
[4] McGuire K, et al. 1983 *Phys. Rev. Lett.* **50** 891.
[5] Chen L, et al. 1984 *Phys. Rev. Lett.* **52** 1122–1125
[6] Heidbrink W W, et al. 1994 *Nuclear Fusion*, **34** 535.
[7] Breizmann B N, et al. 2011 *Nucl. Fusion*, **53** 1.
[8] Zonca F, et al. 2007 *Nucl. Fusion* **47** 1588
[9] Wong M, et al. 2000 *Phys. Rev. Lett.*, **85** 996.
[10] Kadomtsev B B, et al. 1967 *Sov. Physics JETP*, **24** 1172.
[11] Kadomtsev B B, et al. 1971 *Nucl. Fusion*, **11** 67.
[12] Vlad G, et al. 1995 *Physics of Plasmas*, **2** 418-441.
[13] Briguglio S, et al. 1995 *Physics of Plasmas*, **2** 3711-3723.
[14] Briguglio S, et al. 1998 *Physics of Plasmas*, **5** 3287-3301.
[15] Park W, et al. 1992 *Phys. Fluids B* **4** 2033
[16] Izzo R, et al. 1983 *Phys. Fluids* **26** 2240
[17] Wang X, et al. 2011 *Physics of Plasmas*, **18** 052504.
[18] Zonca F, et al. 1996 *Plasma Phys. and Controlled Fusion* **38** 2011
[19] Graves J P, et al. 2000 *Plasma Phys. Control. Fusion* **42** 1049
[20] Zonca F, et al. 2009 *Nuclear Fusion* **49** 085009
[21] Vlad G, et al. 2013 *Nuclear Fusion*, **53** 083008.
[22] White R B 2012 *Commun. Nonlinear Sci. Numer. Simulat.* **17** 2200–2214
[23] Briguglio S, et al. 2014 *Phys. Plasmas*, **21** 112301.
[24] O'Neil T M, et al. 1971 *Phys. Fluids*, **14** 1204.
[25] Chen L, et al. 2016 *Rev. Mod. Phys.* **88** 015008.
[26] Fusco V, et al. 2015 In *14th IAEA Technical Meeting on Energetic Particles in Magnetic Confinement Systems, Wien 1-4 Sept. 2015*, P-28, Vienna, Austria. International Atomic Energy Agency.
[27] Merle A, et al. 2012 *Phys. Plasmas*, **19** 072504.
[28] Kessel C, et al. 1994 *Phys. Rev. Lett.*, **72** 1212.
[29] Zonca F, et al. 2015 *New J. Phys.* **17** 013052.
[30] Wang X, et al. 2016 *Phys. Plasmas*, **23** 012514.
[31] Ponti G., et al. 2014 *Proceedings of the 2014 International Conference on High Performance Computing and Simulation, HPCS 2014*, art. no. 6903807, 1030-1033.